This is the accepted manuscript made available via CHORUS. The article has been published as:

Fast *ab initio* design of high-entropy magnetic materials

Dinesh Bista, Willie B. Beeson, Turbasu Sengupta, Jerome Jackson, Shiv N. Khanna, Kai Liu, and Gen Yin

Phys. Rev. Materials **9**, L031401 — Published 10 March 2025

DOI: 10.1103/PhysRevMaterials.9.L031401

Fast *ab initio* design of high-entropy magnetic materials

Dinesh Bista,[1] Willie B. Beeson,[1] Turbasu Sengupta,[2] Jerome Jackson,[3] Shiv N Khanna,[2] Kai Liu,[1] and Gen Yin[1,*]

[1] *Department of Physics, Georgetown University, Washington, D.C. 20057, USA*
[2] *Department of Physics, Virginia Commonwealth University, Richmond, VA, 23284, USA*
[3] *Scientific Computing Department, STFC Daresbury Laboratory, Warrington WA4 4AD, United Kingdom*

We show that the magnetic properties of high-entropy alloys (HEAs) can be captured by *ab initio* calculations within the coherent potential approximation, where the atomic details of the high-entropy mixing are considered as a uniform effective medium. This is demonstrated using the face-centered cubic (A1) phase of MnFeCoNiCu and the tetragonal ($L1_0$) phase of (MnFeCoNiCu)Pt by comparing the density functional theory (DFT) results with the experimental values. Working within the primitive unit cell of the underlying lattice and its corresponding Brillouin zone, we show that DFT can capture the smooth profile of magnetic properties such as the magnetic moment, the Curie temperature and the magnetic anisotropy, using only a sparse set of sampling points in the vast compositional space. The smooth profiles given by DFT indeed follow the experimental trend, demonstrating the promising potential of using machine learning to explore the magnetic properties of HEAs, by establishing reasonably large datasets with high-throughput DFT calculations.

High-entropy alloys (HEA) are a category of solids with a well-defined underlying crystal lattice, whereas the atomic sites are randomly occupied by the homogeneous, random mixing of five or more different elements[1–10]. After this mixing, the change in the Gibbs free energy $\Delta G = \Delta H - T\Delta S$ is allowed to be negative even with a significant increase in the mixing enthalpy $\Delta H > 0$. This is enabled by the large configurational entropy gain $\Delta S > 0$. Such mixing can thus spontaneously stabilize a crystal structure that hosts many chemical bonds normally not favored in regular intermetallic alloys or ordered crystals[2]. Since the mixing is homogeneous and random, the stabilized crystal becomes a solid solution[5]. Unlike regular ordered alloys, solid solutions host random local strains and lattice distortions because of the complex, multi-element composition. Therefore, atomic diffusion, dislocation, and grain boundary movements are impeded by numerous obstacles. This leads to increased hardness, thermal stability, while surprisingly maintaining good ductility[11, 12]. Similar to the intriguing mechanical properties, solid-solution phases of HEA are also known to possess high chemical stability[8, 13, 14]. Due to the uniform mixing of the high-entropy atomic species, phase segregation in HEAs is more suppressed compared to regular alloys. This impedes the progress of electrochemical processes and thereby enhances the robustness against bimetallic corrosion. Due to these intriguing properties, HEAs have undergone extensive investigation, primarily focused on their enhanced mechanical and chemical properties [6, 15–17]. Recent developments in machine learning and autonomous workflow have brought both the experimental and theoretical research to a new level[18–21].

In addition to mechanical and chemical robustness, HEAs can also exhibit exceptional magnetic properties[15, 22–26]. The ordered structures of HEAs, especially the $L1_0$ -phase, naturally break the $SO(3)$ symmetry, allowing for good magnetic anisotropy. Also, the random local distortion of the lattice can serve as pinning sites, resulting in good permanent magnets with large coercivity[27]. Due to the compositional complexity, it is possible to modulate the key magnetic properties such as the magnetic moment per unit cell (μ_{cell}), the magnetic anisotropy energy density (MAE) and the Curie temperature (T_C) in a reasonably large range[17, 28]. This provides the opportunity to identify ideal media for advanced technologies such as heat- or microwave-assisted magnetic recording (HAMR and MAMR), where fine-tuning of μ_{cell}, MAE and T_C are needed to identify the best balance among the recording trilemma for each generation of the technology[29–35]. This calls for the investigation of magnetic properties of thin-film HEAs in their vast, high-dimensional compositional space.

Here, we demonstrate the design principle for magnetic properties of thin-film HEAs using density-functional theory (DFT). By comparing to experimental results, we demonstrate that bulk DFT calculations using experimental thin-film lattice constants can capture the smooth profile of magnetic properties in the high-entropy compositional space. Specifically, we demonstrate this design principle for the MAE of two thin-film HEAs that have been recently achieved experimentally: the face-centered cubic (FCC, or A1) phase of MnFeCoNiCu and the $L1_0$ phase of (MnFeCoNiCu)Pt, where robust solid solutions with large MAE and exceptional crystallization have been identified[36]. Particularly, we show that the first-principles calculation can be carried out efficiently at the level of coherent-potential approximation (CPA), a method that can capture the Green's function of disordered systems, allowing for fast and accurate evaluation of electronic and magnetic properties of random alloys without the necessity of sampling different configurations using supercells[37–39]. This illustrates the possibility of using machine-learning models to make reasonable predictions once a large-scale database is established.

The *ab initio* calculations in this work are performed

* gen.yin@georgetown.edu

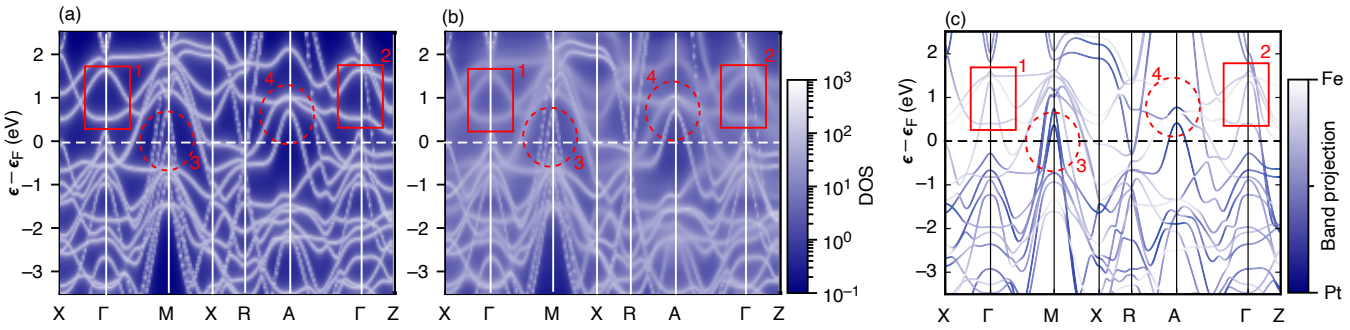


Fig 1. (a) The Spectral function of $L1_0$-phase FePt obtained by the Green's function implementation of DFT in Questaal. Coherent potential approximation was used assuming no random mixing to resolve the band structure. An overall broadening energy of 0.001 Ryd was applied to visualize the spectral function. (b) The spectral function in the case of $[Fe_{0.8}(MnCoNiCu)_{0.2}]Pt$ with the random mixing slightly turned on for Fe sites. (c) The VASP result of pure FePt with eigenstates projected to Fe and Pt orbitals. The weight of the projection is denoted by the color scale. The energy cutoff was set to 400 eV, and the DFT-D3 dispersion correction with Becke-Johnson damping was used[40–42]. A Γ-centered $12 \times 12 \times 9$ mesh was used for the k-space integration. The convergence criterion was set to 10^{-7} eV.

using the Green's function formulation of DFT and Linear Muffin Tin Orbitals (LMTOs) within the atomic-sphere approximation (ASA). To model the irregularities in HEAs, we perform spin-polarized self-consistent calculations using the CPA implemented by the 'lmgf' package in the Questaal suite [43]. This approximation considers the irregularities as an averaged effective medium, allowing us to work within the primitive unit cell associated with the underlying lattice type. The electron density is obtained by integrating over a Γ-centered $16 \times 16 \times 16$ k-mesh[44] and 25 energy points uniformly distributed along an elliptical contour of 0.4 eccentricity, covering the energy range of 0.85 Ryd below the Fermi level ϵ_F. The value of ϵ_F is determined by the charge-neutrality condition as implemented in the package. The third-order potential function approximation (p_3) and the convergence criterion of 10^{-6} Ryd are used. For the calculations of μ_{cell}, the magnetic moment per unit cell in the converged ground state is taken. Spin-orbit coupling is considered as a $\langle L{\cdot}S \rangle$ term added to the one-body Hamiltonian when calculating the MAE. The values of MAE are extracted by comparing the converged ground-state energy and another single-step energy using the converged moments in the previous step, but rotating the spin quantization axis from the easy axis to a perpendicular direction. The specific choices of quantization directions are made according to the setup of experiments.

We first verify our calculations by aligning Questaal results with other DFT implementations and experimental data. This comparison focuses on the well-known high anisotropy single crystal FePt in the $L1_0$ phase. The primitive cell of the $L1_0$ phase is tetragonal, with Fe atoms occupying the corners and the Pt atom at the body center. Assuming 100% occupation of both Fe and Pt sites in the CPA setup, the calculation goes back to a DFT calculation of a pure system, which should recover the band structure obtained by other DFT implementations such as VASP[45, 46]. In both calculations, we use $a = 2.69$ Å and $c = 3.69$ Å as the lattice constants. Perdew-Burke-Ernzerhof (PBE) type of generalized gradient approximation (GGA) is used as the exchange-correlation functional[47]. The spectral function $A(\epsilon, \mathbf{k})$ along the high-symmetry route is illustrated in Fig. 1(a). This electron spectrum changes significantly when the high-entropy random mixing was slightly turned on for the Fe sites, that is, reducing the probability of the Fe occupation to 0.8 while simultaneously turning on the probability of $(MnCoNiCu)_{0.2}$ accordingly.

To compare to the Questaal results, the eigenvalues of the Kohn-Sham Hamiltonian obtained by VASP are illustrated along the same high symmetry route, as shown in Fig. 1(c). Although there are discrepancies in some details, the Questaal spectrum agrees with the VASP bands generally. Due to the random scattering, although all bands are smeared due to the finite life time, different eigenstates have different levels of broadening. To show this, four representative spectra are highlighted in Figs. 1(a-c). In all four cases, the band smearing mainly occurs for the Fe-dominated bands, whereas the Pt bands remain sharp. This is consistent with the fact that the body-center sites are uniformly occupied by Pt atoms without any random mixing. After this verification, we further calculate the magnetic moment per unit cell and the MAE for $L1_0$ FePt and compare the results with experiments, as shown in Table I. We used both PBE-GGA and local density approximation (LDA)[48]. The calculated μ_{cell} from the Questaal matches closely with the experimental and the VASP results[49]. For MAE, DFT appears to overestimate the experimental value for all of the performed calculations, as observed in both VASP and Questaal calculations.

The magnetic properties of high-entropy alloys are analyzed using the CPA, which models random alloys by accounting for the occupation probabilities of each element

Table I. Comparison of MAE and μ_{cell} for pure $L1_0$-FePt.

Method	MAE(MJ/m^3)	$\mu_{\text{cell}}(\mu_B)$
Experiment[50, 51]	(6.6-10)	3.34 ± 0.034
VASP (LDA)[49]	17.8	3.06
Questaal (LDA)	16.5	3.26
VASP (GGA)[49]	15.7	3.22
Questaal (GGA)	15.6	3.33

at each lattice site. This allows us to compute different alloy compositions and evaluate magnetic ordering at zero temperature. CPA provides an effective medium based on site occupation concentrations and is used to study magnetic ordering. We computed the magnetocrystalline anisotropy energy by considering total energy differences with spin-orbit interactions, using the zero-temperature CPA ground state.

To account for magnetic disorder, we applied the disordered local moment (DLM) theory. This theory describes the paramagnetic phase at high temperatures, where no Weiss field is present, meaning magnetic moments only arise when locally sustained. Without spin-orbit coupling (SOC), the DLM model simplifies to a 50:50 mix of spin-up and spin-down states, known as the alloy analogy model[52, 53]. We used this model to estimate the critical temperature by comparing the paramagnetic phase energy with the zero-temperature ground state, providing an upper bound in our DFT-based estimate.

In our study of MnFeCoNiCu, using the primitive unit cell and single-spin CPA sites without SOC, we found a ferrimagnetic ground state with a saturation magnetization of 34 emu/g, far below the previously reported 81 emu/g[54] and 75 emu/g[36]. Previous studies[54] show that the layered Mn antiferromagnetic (AFM) state is the true ground state. Our CPA calculations in the primitive unit cell failed to capture long-range interactions like the layered Mn AFM configuration. However, applying a conventional unit cell approach, we confirmed the layered Mn AFM ground state.

Next, we introduced a split spin-up and spin-down configuration at the Mn CPA site within the primitive unit cell while assigning single spin at all other CPA sites, and this yielded identical results with the conventional unit cell calculations, such as the layered Mn AFM state being the magnetic ground state. The local magnetic moments for each CPA site also closely matched those from the conventional unit cell calculations. For instance, using LDA, the magnetic moments were converged to Mn: -0.08 (averaging Mn up-spin and down-spin), Fe: 2.32, Co: 1.38, Ni: 0.40, and Cu: 0.04 in units of μ_B, resulting in a net $\mu_{\text{cell}} = 0.81\,\mu_{\text{B}}$. Using GGA, the net moment was $\mu_{\text{cell}} = 0.86\,\mu_{\text{B}}$. In both cases, species were found to be ferromagnetically aligned in the zero-temperature ground state, except for Mn, where a mixture of up and down spins with almost equal probability was identified. These results are consistent with prior DFT studies using CPA, DLM, and supercells[54]. Finally, due to the computational efficiency of this approach, especially when exploring the vast compositional space of high-entropy alloys and for designing models, we opted to use the primitive unit cell calculations with spin-up and spin-down configurations at the Mn CPA sites. This method not only captures essential magnetic behaviors but also serves as a practical tool for HEA design and analysis for finding the magnetic ground state and reporting the ground state magnetic details like μ_{cell}.

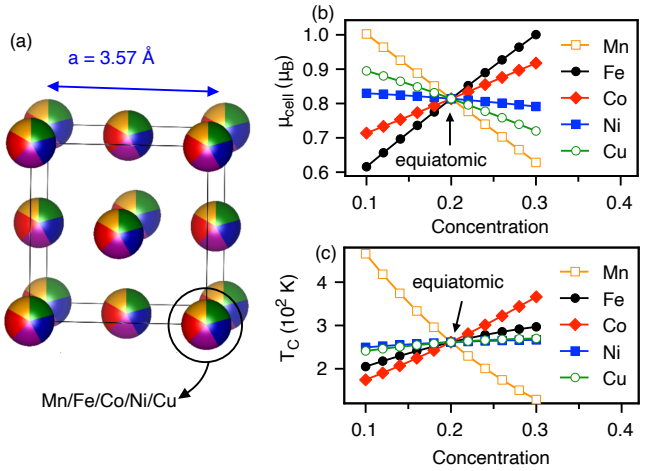


Fig 2. Magnetic properties of the high-entropy crystal MnFeCoNiCu in the A1 phase. (a) The conventional FCC unit cell with all atomic sites randomly occupied by the five different elements. (b) The magnetic moment per unit cell (μ_{cell}) when modulating the concentration of one high-entropy element. All other high-entropy elements are adjusted proportionately to maintain a total concentration of 100%. The central composition of 0.2 corresponds to the equiatomic case. (c) The modulation of Curie temperature corresponding to changes in the concentration of one element, according to the pattern described in (b).

To capture the landscape of μ_{cell} near the equiatomic case, we further explore the compositional space by varying the concentration of one high-entropy element, whereas simultaneously changing the concentration of others accordingly, keeping the total occupation probability normalized. The LDA results are shown in Fig. 2(b). Here, μ_{cell} increases with the Fe and Co concentration, whereas extra mixing of Mn and Cu decreases the μ_{cell} significantly. This is expected since Mn is found to have a mixture of both positive and negative spins, whereas Cu atoms are non-magnetic.

After exploring the magnetic ordering of equiatomic recipe, we estimate the ordering temperature (T_C) through mean-field approximation.[55–57]:

$$T_C = \frac{2(\epsilon_{\text{PM}} - \epsilon_{\text{GS}})}{3(1-c)k_{\text{B}}}, \tag{1}$$

where ϵ_{PM} and ϵ_{GS} represent converged energies of paramagnetic and ground-state spin configurations, respectively. Here, k_{B} is the Boltzmann constant and c denotes the net concentration of the non-magnetic atoms in the

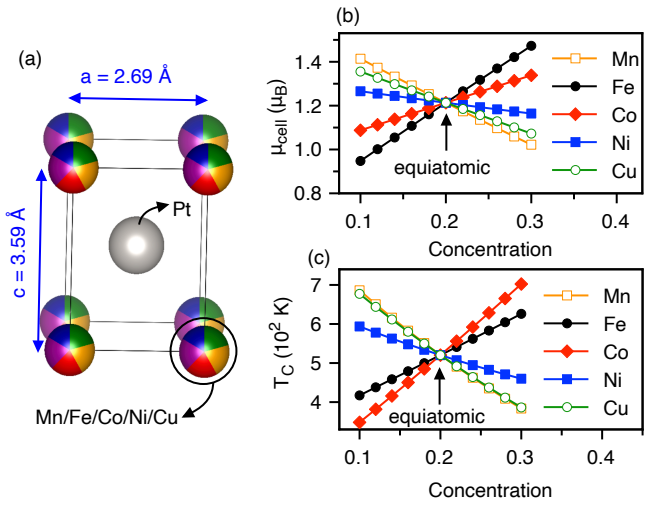


Fig 3. The magnetic moment per unit cell and the Curie temperature of high-entropy magnet (MnFeCoNiCu)Pt in the $L1_0$ phase. (a) The primitive unit cell of the tetragonal lattice. (b) The magnetic moment per unit cell when modulating the concentration of one high-entropy element on the corner sites. All other corner sites are adjusted proportionately to maintain a total concentration of 100%. The body-center Pt site is assumed to be uniformly occupied. The 20% concentration corresponds to the equiatomic case for all the corner sites. (c) The modulation of Curie temperature corresponding to changes in the concentration of one element, following the pattern described in (b).

HEA. Note that Eq. 1 is a crude approximation for estimating the upper limit[55]. The estimated T_C for the equiatomic case using LDA and GGA are found to be 261 K and 359 K, respectively, which are close to existing DFT results[54]. We then explore the landscape of T_C in the compositional space near the equiatomic recipe by varying the concentrations similar to that used for μ_{cell}. The LDA results are summarized in Fig. 2(c), where T_C decreases significantly with the increase in the Mn concentration. This is consistent with the fact that the ground-state Mn atoms have a mixing of both positive and negative spins, suggesting that their exchange couplings with other high-entropy species should be antiferromagnetic.

To understand the MAE of MnFeCoNiCu in its A1 (FCC) solid solution phase, we compare the ground-state energy when the spin quantization axis is along different directions. Care must be taken since the MAE is only a small fraction of the total energy. To evaluate the limit of our numerical resolution, we first examine the energy difference between two equivalent directions within the $\langle 100 \rangle$ family, where the energy difference should be exactly 0. With a convergence criterion of 10^{-6} Ryd, the numerical difference between [001] and [100] magnetization corresponds to $\sim 0.182\,\text{MJ/m}^3$. This value will be used as our numerical limit to resolve the MAE calculation. We then examine the MAE value taking [111] and [110] as the easy and hard axes, respectively, which resulted in an MAE of $0.201\,\text{MJ/m}^3$. This is close to the resolution of our calculation, and we therefore conclude that the MAE between [111] and [110] is beyond the numerical accuracy of our calculation. Note that this energy difference is indeed detectable in experiments[36]. The small MAE is a consequence of the highly symmetric cubical lattice, as well as the lack of heavy elements providing a sizable SOC. To increase the MAE, we further mix Pt into the FCC solid solution by replacing Mn[58], which is known to couple to other high-entropy species antiferromagnetically. Keeping the lattice constant the same to the case of MnFeCoNiCu, the MAE with the Pt mixing remains close to our numerical resolution ($\sim 0.1\,\text{MJ/m}^3$). This suggests that further breaking the symmetries of the cubical lattice may be necessary to increase the MAE.

One way to break the symmetry of the A1 (FCC) lattice is to insert a layer of Pt atoms between the high-entropy layers stacking along the c axis. The change in the c axis brings the FCC lattice to a tetragonal one, as shown by Fig. 3(a). Pure crystals of this phase is well known to host large MAE in many different cases such as FePt, CoPt and MnAl[59–61]. Recently, this $L1_0$ phase of (MnFeCoNiCu)Pt has been experimentally realized through a co-sputtering followed by a rapid thermal annealing, where both good crystallization and large MAE have been confirmed[34, 36, 62].

According to the experimental characterization, we assume that there is no random mixing for the Pt atoms at the body-center sites, whereas all corner sites are occupied by the high-entropy mixing of the transition metal elements. This assures that the strong SOC given by the Pt atoms is homogeneously experienced by all the transition metal elements. Using the experimental lattice constants listed in Fig. 3(a), we explore the magnetic properties of (MnFeCoNiCu)Pt in the compositional space, and the results are shown in Figs. 3(b-c). Compared to the FCC structure, the magnetic moment per unit cell decreases near the equiatomic composition due to the incorporation of non-magnetic Pt. Unlike the equiatomic FCC case, all compositions we explored for the $L1_0$ phase have a ferromagnetic ground state, resulting in a significant increase of ~ 200 K in T_C. Increasing the concentrations of Fe and Co increases both μ_{cell} and T_C, whereas the mixing of Mn and Cu has an opposite trend. This suggests a potential engineering strategy to reduce the writing power for HAMR devices.

We use machine learning to explore the MAE of the $L1_0$ phase, resulting in a smooth profile in the compositional space that is consistent with the experimental trend. Similar to the previous cases, we first modulate the compositions near the equiatomic case for the transition metals, while keeping Pt fixed at 50%. For all explored cases, DFT suggests that the [001] direction is an easier axis compared to [100], and the MAE values are shown in Fig. 4(a). Although this result suggests significant correlation between the Fe concentration and the MAE, it is clear that all transition-metal

Table II. Elemental compositions of the samples.

Samples	Compositions
1	$Mn_{0.11}Fe_{0.07}Co_{0.12}Ni_{0.11}Cu_{0.12}Pt_{0.47}$
2	$Mn_{0.07}Fe_{0.10}Co_{0.08}Ni_{0.20}Cu_{0.09}Pt_{0.46}$
3	$Mn_{0.09}Fe_{0.11}Co_{0.09}Ni_{0.10}Cu_{0.11}Pt_{0.50}$
4	$Mn_{0.09}Fe_{0.13}Co_{0.11}Ni_{0.07}Cu_{0.11}Pt_{0.49}$
5	$Mn_{0.07}Fe_{0.19}Co_{0.10}Ni_{0.10}Cu_{0.08}Pt_{0.46}$

elements have strong influences. To fully capture and visualize the MAE profile, we use machine learning and interpolation in the compositional space. This is implemented using multidimensional scaling (MDS), an unsupervised learning method typically used to cluster high-dimensional points [63]. MDS searches for an optimal curved 2-dimensional surface in a high (6 in our case) dimensional parameter space, such that the points can uniformly scale their Euclidean distance to their neighbors after projected onto the surface. This surface is numerically described by a discrete manifold, which can be illustrated on a flat 2D plane after a straightforward transformation.

The flattened MDS map of the data points in Fig.4(a) is illustrated in Fig.4(b), with the projected locations denoted by the crosses. The MAE values obtained by DFT are illustrated with the white-salmon color scale, where the empty space between points are filled using Hermite-Zero-Derivative Start (HZDS) interpolation. The DFT results are compared with experiments using five different $L1_0$ thin films near the equiatomic composition. These samples were fabricated and characterized using the same approach described in our previous work[36], where the compositions are estimated by Energy-Dispersive X-Ray Spectroscopy (EDS) and the MAE values estimated by magnetometry measurements at 5K to have fair comparison with DFT results. The specific compositions of these five samples are listed in Table II. These compositions are projected to the same MDS manifold, which are illustrated by the solid circles in Fig. 4(b) where the white-blue scale represents the normalized experimental values. It can be seen that the general trend of the experimental MAE is highly correlated to the interpolated MDS profile. We also performed DFT calculations using the experimental compositions of the five samples. Except for Sample 3, high entropy elements occupy the Pt-sites in all other samples, with Pt-site occupation slightly below 50%. In DFT calculations, various permutations of high-entropy elements on Pt-sites are explored. To manage the exhaustive possibilities, an unbiased subset is selected, ensuring equal representation of all five high-entropy elements. The average MAE and μ_{cell} are then calculated from this subset, and the results are shown in Figs. 4(c-d). The uncertainties due to unknown mixing of high entropy elements on the Pt sites are reflected in the DFT error bars, while the experimental error bars represent the uncertainties in the magnetometry measurements. For the magnetic moment, the DFT values are systematically greater than the experimental ones by a factor of ~ 2. In terms of the trend, the experimental μ_{cell} of Sample 2 is larger than that of Samples 1 and 3, while DFT suggests that the μ_{cell} of sample 1 is slightly greater than that of sample 2.

Unlike the magnetic moment, the numerical trend of MAE values given by DFT and experiments are consistent among all five samples. In all cases, DFT systematically overestimates the MAE by at least several factors, and the discrepancies are greater than the ones seen in pure FePt (Table I). The systematic overestimation of MAE by DFT is likely induced by the assumption of perfect crystallization, whereas the real samples have complicated grain landscapes and lattice distortions that are difficult to capture by the DFT setup. For our CPA calculations, this overestimation may also stem from the mean-field approximation in CPA, where short-range ordering and local atomic-structure reorganization are ignored. Although quantitative agreement between theory and experiment is difficult, the trend of MAE is consistent with the experimental ones among all five samples. Note that the DFT calculated MAE values for the experimental compositions are not used in the interpolation shown in Fig. 4(b), suggesting that the smooth profile of the MAE can be captured by the sparse points sampled in the compositional space.

The results shown above suggest that sparse sampling in the compositional space of HEAs using primitive-cell DFT calculations can capture the trend of magnetic properties including μ_{cell}, MAE and T_C, even after losing the information of atomic occupation details within CPA. Since CPA assumes a fixed underlying lattice but accounts for local single-site scattering due to compositional or magnetic disorders, the Green's functions are naturally diagonal in $\mathbf{k}$, allowing for the fast evaluation of the electron density by working only with the primitive cell. Although the experiments do not quantitatively agree with DFT, the profile in the high-dimensional compositional space is smooth, which can be captured by a reasonable number of discrete points sparsely sampled in the compositional space. This invites further research to establish large-scale databases within the mean-field approximation of CPA to establish predictive machine-learning models. This also introduces an intriguing opportunity to achieve the fast design of future high-entropy magnets for many scenarios of application.

Acknowledgments: This paper is based upon work supported by the National Science Foundation (US) under Grant No. ECCS-2151809. This work used Bridges-2 at Pittsburgh Supercomputing Center through allocation PHY230018 from the Advanced Cyberinfrastructure Coordination Ecosystem: Services & Support (ACCESS) program, which is supported by National Science Foundation (US) grants #2138259, #2138286, #2138307, #2137603, and #2138296. The acquisition of the MPMS3 system used in this study was supported by the NSF-MRI program (DMR-1828420). TS and SNK gratefully acknowledge funding from US Department of

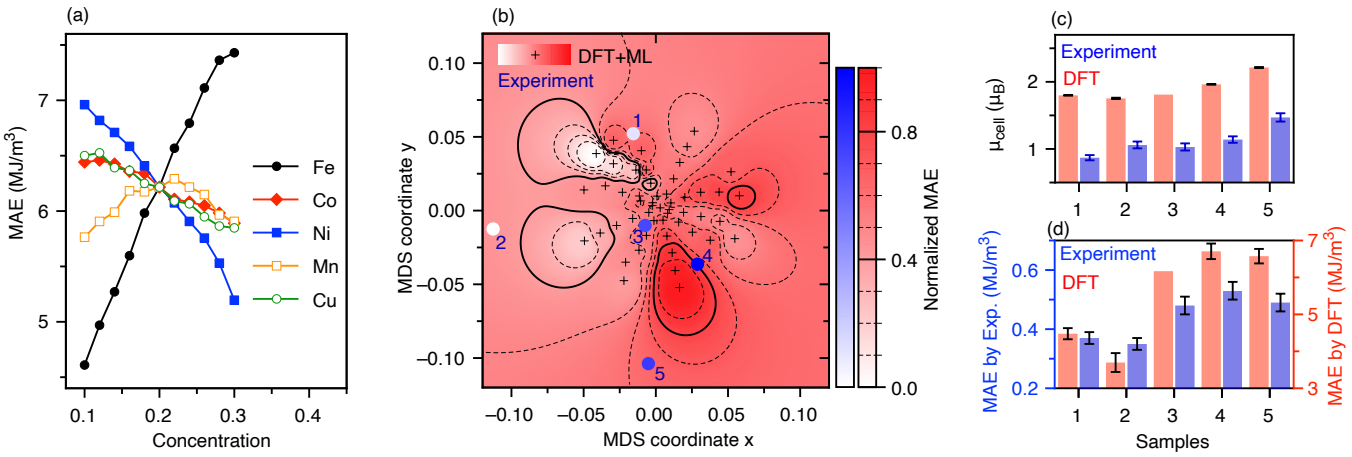


Fig 4. The magnetic anisotropy energy density (MAE) of the $L1_0$ high-entropy magnet (MnFeCoNiCu)Pt. (a) The variation of MAE for different compositions when each high entropy element is modulated following the pattern described in Figs. 2 and 3. (b) The compositions in (a) projected from $\mathbb{R}^6$ to $\mathbb{R}^2$ using Multidimensional Scaling (MDS), which preserves the Euclidean distances between points. Color saturation denotes the MAE values scaled between 0 and 1. The red and blue points denote the DFT and the experimental results, respectively. (c-d) Direct comparison between the theoretical and experimental results for the 5 samples highlighted in (b). Here the μ_{cell} comparison is shown in (c), whereas the MAE comparison is shown in (d). Note that μ_{cell} is compared with the same scale in (c), whereas the MAE comparison is illustrated on different scales in (d).

Energy (DOE), under the award DE-SC0006420. JJ acknowledges support under the CCP9 project "Computational Electronic Structure of Condensed Matter"(part of Computational Science Centre of Research Communities(CoSeC)).

[1] Y. Zhang, T. T. Zuo, Z. Tang, M. C. Gao, K. A. Dahmen, P. K. Liaw, and Z. P. Lu, Microstructures and properties of high-entropy alloys, Prog. Mater. Sci. **61**, 1 (2014).
[2] J.-W. Yeh, S.-J. Lin, T.-S. Chin, J.-Y. Gan, S.-K. Chen, T.-T. Shun, C.-H. Tsau, and S.-Y. Chou, Formation of simple crystal structures in Cu-Co-Ni-Cr-Al-Fe-Ti-V alloys with multiprincipal metallic elements, Met. Mater Trans A **35**, 2533 (2004).
[3] T. K. Chen, T. T. Shun, J. W. Yeh, and M. S. Wong, Nanostructured nitride films of multi-element high-entropy alloys by reactive DC sputtering, Surf. Coat. Tech. **188–189**, 193 (2004).
[4] B. Cantor, I. T. H. Chang, P. Knight, and A. J. B. Vincent, Microstructural development in equiatomic multicomponent alloys, Mater. Sci. Eng. A **375–377**, 213 (2004).
[5] J.-W. Yeh, S.-K. Chen, S.-J. Lin, J.-Y. Gan, T.-S. Chin, T.-T. Shun, C.-H. Tsau, and S.-Y. Chang, Nanostructured High-Entropy Alloys with Multiple Principal Elements: Novel Alloy Design Concepts and Outcomes, Adv. Eng. Mater. **6**, 299 (2004).
[6] D. B. Miracle and O. N. Senkov, A critical review of high entropy alloys and related concepts, Acta Mater. **122**, 448 (2017).
[7] E. P. George, W. A. Curtin, and C. C. Tasan, High entropy alloys: A focused review of mechanical properties and deformation mechanisms, Acta Mater. **188**, 435 (2020).
[8] E. P. George, D. Raabe, and R. O. Ritchie, High-entropy alloys, Nat. Rev. Mater. **4**, 515 (2019).
[9] R. Kozak, A. Sologubenko, and W. Steurer, Single-phase high-entropy alloys – an overview, Z Krist. Cryst Mater **230**, 55 (2015).
[10] S. Praveen and H. S. Kim, High-Entropy Alloys: Potential Candidates for High-Temperature Applications - An Overview, Adv. Eng. Mater. **20**, 1700645 (2018).
[11] Z. Lei, X. Liu, Y. Wu, H. Wang, S. Jiang, S. Wang, X. Hui, Y. Wu, B. Gault, P. Kontis, D. Raabe, L. Gu, Q. Zhang, H. Chen, H. Wang, J. Liu, K. An, Q. Zeng, T.-G. Nieh, and Z. Lu, Enhanced strength and ductility in a high-entropy alloy via ordered oxygen complexes, Nature **563**, 546 (2018).
[12] W. Li, D. Xie, D. Li, Y. Zhang, Y. Gao, and P. K. Liaw, Mechanical behavior of high-entropy alloys, Prog. Mater. Sci. **118**, 100777 (2021).
[13] Y. Y. Chen, T. Duval, U. D. Hung, J. W. Yeh, and H. C. Shih, Microstructure and electrochemical properties of high entropy alloys—a comparison with type-304 stainless steel, Corros. Sci. **47**, 2257 (2005).
[14] C. P. Lee, Y. Y. Chen, C. Y. Hsu, J. W. Yeh, and H. C. Shih, The Effect of Boron on the Corrosion Resistance of the High Entropy Alloys $Al_{0.5}CoCrCuFeNiB_x$, J. Electrochem. Soc. **154**, C424 (2007).
[15] J. Y. Law and V. Franco, Review on magnetocaloric high-entropy alloys: Design and analysis methods, J. Mater. Res. **38**, 37 (2023).
[16] M. Vaidya, G. M. Muralikrishna, and B. S. Murty, High-entropy alloys by mechanical alloying: A review, J.

Mater. Res. **34**, 664 (2019).
[17] Y. F. Ye, Q. Wang, J. Lu, C. T. Liu, and Y. Yang, High-entropy alloy: Challenges and prospects, Mater. Today **19**, 349 (2016).
[18] Z. Rao, P.-Y. Tung, R. Xie, Y. Wei, H. Zhang, A. Ferrari, T. Klaver, F. Körmann, P. T. Sukumar, A. Kwiatkowski da Silva, Y. Chen, Z. Li, D. Ponge, J. Neugebauer, O. Gutfleisch, S. Bauer, and D. Raabe, Machine learning–enabled high-entropy alloy discovery, Science **378**, 78 (2022).
[19] S. Divilov, H. Eckert, D. Hicks, C. Oses, C. Toher, R. Friedrich, M. Esters, M. J. Mehl, A. C. Zettel, Y. Lederer, E. Zurek, J.-P. Maria, D. W. Brenner, X. Campilongo, S. Filipović, W. G. Fahrenholtz, C. J. Ryan, C. M. DeSalle, R. J. Crealese, D. E. Wolfe, A. Calzolari, and S. Curtarolo, Disordered enthalpy–entropy descriptor for high-entropy ceramics discovery, Nature **625**, 66 (2024).
[20] W. Huang, P. Martin, and H. L. Zhuang, Machine-learning phase prediction of high-entropy alloys, Acta Mater. **169**, 225 (2019).
[21] C. Oses, E. Gossett, D. Hicks, F. Rose, M. J. Mehl, E. Perim, I. Takeuchi, S. Sanvito, M. Scheffler, Y. Lederer, O. Levy, C. Toher, and S. Curtarolo, AFLOW-CHULL: Cloud-Oriented Platform for Autonomous Phase Stability Analysis, J. Chem. Inf. Model. **58**, 2477 (2018).
[22] J. Wang, Z. Zheng, J. Xu, and Y. Wang, Microstructure and magnetic properties of mechanically alloyed FeSiBAlNi (Nb) high entropy alloys, J. Magn. Magn. Mater. **355**, 58 (2014).
[23] L. Liu, J. B. Zhu, J. C. Li, and Q. Jiang, Microstructure and Magnetic Properties of $FeNiCuMnTiSn_x$ High Entropy Alloys, Adv. Eng. Mater. **14**, 919 (2012).
[24] N. Tang, L. Quigley, W. L. Boldman, C. S. Jorgensen, R. Koch, D. O'Leary, H. R. Medal, P. D. Rack, and D. A. Gilbert, Magnetism in metastable and annealed compositionally complex alloys, Phys. Rev. Mater. **5**, 114405 (2021).
[25] C. D. Woodgate, D. Hedlund, L. H. Lewis, and J. B. Staunton, Interplay between magnetism and short-range order in medium- and high-entropy alloys: Crconi, crfeconi, and crmnfeconi, Phys. Rev. Mater. **7**, 053801 (2023).
[26] D. Billington, A. D. N. James, E. I. Harris-Lee, D. A. Lagos, D. O'Neill, N. Tsuda, K. Toyoki, Y. Kotani, T. Nakamura, H. Bei, S. Mu, G. D. Samolyuk, G. M. Stocks, J. A. Duffy, J. W. Taylor, S. R. Giblin, and S. B. Dugdale, Bulk and element-specific magnetism of medium-entropy and high-entropy cantor-wu alloys, Phys. Rev. B **102**, 174405 (2020).
[27] S.-M. Na, P. K. Lambert, and N. J. Jones, Hard magnetic properties of $FeCoNiAlCu_XTi_X$ based high entropy alloys, AIP Adv. **11**, 015210 (2021).
[28] P. Kumari, A. K. Gupta, R. K. Mishra, M. Ahmad, and R. R. Shahi, A Comprehensive Review: Recent Progress on Magnetic High Entropy Alloys and Oxides, J. Magn. Magn. Mater. **554**, 169142 (2022).
[29] D. Weller and A. Moser, Thermal effect limits in ultrahigh-density magnetic recording, IEEE Trans. Magn. **35**, 4423 (1999).
[30] R. Rottmayer, S. Batra, D. Buechel, W. Challener, J. Hohlfeld, Y. Kubota, L. Li, B. Lu, C. Mihalcea, K. Mountfield, K. Pelhos, C. Peng, T. Rausch, M. Seigler, D. Weller, and X.-M. Yang, Heat-Assisted Magnetic Recording, IEEE Trans. Magn. **42**, 2417 (2006).
[31] D. Weller, G. Parker, O. Mosendz, A. Lyberatos, D. Mitin, N. Y. Safonova, and M. Albrecht, Review Article: FePt heat assisted magnetic recording media, J. Vac. Sci. Technol. B **34**, 060801 (2016).
[32] J. E. Davies, O. Hellwig, E. E. Fullerton, G. Denbeaux, J. B. Kortright, and K. Liu, Magnetization reversal of Co/Pt multilayers: Microscopic origin of high-field magnetic irreversibility, Phys. Rev. B **70**, 224434 (2004).
[33] M. T. Rahman, R. K. Dumas, N. Eibagi, N. N. Shams, Y.-C. Wu, K. Liu, and C.-H. Lai, Controlling magnetization reversal in Co/Pt nanostructures with perpendicular anisotropy, Appl. Phys. Lett. **94**, 042507 (2009).
[34] D. A. Gilbert, L.-W. Wang, T. J. Klemmer, J.-U. Thiele, C.-H. Lai, and K. Liu, Tuning magnetic anisotropy in (001) oriented $L1_0$ $(Fe_{1-x}Cu_x)_{55}Pt_{45}$ films, Appl. Phys. Lett. **102**, 132406 (2013).
[35] R. Cuadrado, K. Liu, T. J. Klemmer, and R. W. Chantrell, In-plane/out-of-plane disorder influence on the magnetic anisotropy of $Fe_{1-y}Mn_yPt$-$L1_0$ bulk alloy, Appl. Phys. Lett. **108**, 123102 (2016).
[36] W. B. Beeson, D. Bista, H. Zhang, S. Krylyuk, A. V. Davydov, G. Yin, and K. Liu, Single-phase L10-ordered high entropy thin films with high magnetic anisotropy, Advanced Science **11**, 2308574 (2024).
[37] P. Soven, Coherent-Potential Model of Substitutional Disordered Alloys, Phys. Rev. **156**, 809 (1967).
[38] P. Soven, Contribution to the Theory of Disordered Alloys, Phys. Rev. **178**, 1136 (1969).
[39] C. D. Woodgate and J. B. Staunton, Compositional phase stability in medium-entropy and high-entropy Cantor-Wu alloys from an ab initio all-electron Landau-type theory and atomistic modeling, Phys. Rev. B **105**, 115124 (2022).
[40] S. Grimme, J. Antony, S. Ehrlich, and H. Krieg, A consistent and accurate ab initio parametrization of density functional dispersion correction (DFT-D) for the 94 elements H-Pu, J. Chem. Phys. **132**, 154104 (2010).
[41] A. D. Becke and E. R. Johnson, A density-functional model of the dispersion interaction, J. Chem. Phys. **123**, 154101 (2005).
[42] S. Grimme, S. Ehrlich, and L. Goerigk, Effect of the damping function in dispersion corrected density functional theory, J. Comput. Chem. **32**, 1456 (2011).
[43] D. Pashov, S. Acharya, W. R. Lambrecht, J. Jackson, K. D. Belashchenko, A. Chantis, F. Jamet, and M. van Schilfgaarde, Questaal: A package of electronic structure methods based on the linear muffin-tin orbital technique, Comput. Phys. Commun. **249**, 107065 (2020).
[44] H. J. Monkhorst and J. D. Pack, Special points for Brillouin-zone integrations, Phys. Rev. B **13**, 5188 (1976).
[45] G. Kresse and J. Furthmüller, Efficiency of ab-initio total energy calculations for metals and semiconductors using a plane-wave basis set, Comput. Mater. Sci. **6**, 15 (1996).
[46] G. Kresse and J. Furthmüller, Efficient iterative schemes for ab initio total-energy calculations using a plane-wave basis set, Phys. Rev. B **54**, 11169 (1996).
[47] J. P. Perdew, K. Burke, and M. Ernzerhof, Generalized gradient approximation made simple, Phys. Rev. Lett. **77**, 3865 (1996).
[48] U. von Barth and L. Hedin, A local exchange-correlation potential for the spin polarized case. I, J. Phys. C: Solid State Phys. **5**, 1629 (1972).

[49] M. Wolloch, D. Suess, and P. Mohn, Influence of antisite defects and stacking faults on the magnetocrystalline anisotropy of FePt, Phys. Rev. B **96**, 104408 (2017).

[50] T. Klemmer, D. Hoydick, H. Okumura, B. Zhang, and W. A. Soffa, Magnetic hardening and coercivity mechanisms in $L1_0$ ordered FePd ferromagnets, Scr. Mater. **33**, 1793 (1995).

[51] D. Weller, A. Moser, L. Folks, M. Best, W. Lee, M. Toney, M. Schwickert, J.-U. Thiele, and M. Doerner, High K_u materials approach to 100 Gbits/in^2, IEEE Trans. Magn. **36**, 10 (2000).

[52] J. Staunton, B. L. Gyorffy, G. M. Stocks, and J. Wadsworth, The static, paramagnetic, spin susceptibility of metals at finite temperatures, Journal of Physics F: Metal Physics **16**, 1761 (1986).

[53] B. L. Gyorffy, A. J. Pindor, J. Staunton, G. M. Stocks, and H. Winter, A first-principles theory of ferromagnetic phase transitions in metals, Journal of Physics F: Metal Physics **15**, 1337 (1985).

[54] Z. Rao, B. Dutta, F. Körmann, D. Ponge, L. Li, J. He, L. Stephenson, L. Schäfer, K. Skokov, O. Gutfleisch, D. Raabe, and Z. Li, Unveiling the mechanism of abnormal magnetic behavior of FeNiCoMnCu high-entropy alloys through a joint experimental-theoretical study, Phys. Rev. Mater. **4**, 014402 (2020).

[55] K. Sato, L. Bergqvist, J. Kudrnovský, P. H. Dederichs, O. Eriksson, I. Turek, B. Sanyal, G. Bouzerar, H. Katayama-Yoshida, V. A. Dinh, T. Fukushima, H. Kizaki, and R. Zeller, First-principles theory of dilute magnetic semiconductors, Rev. Mod. Phys. **82**, 1633 (2010).

[56] F. Körmann, D. Ma, D. D. Belyea, M. S. Lucas, C. W. Miller, B. Grabowski, and M. H. F. Sluiter, "Treasure maps" for magnetic high-entropy-alloys from theory and experiment, Appl. Phys. Lett. **107**, 142404 (2015).

[57] K. Sato, P. H. Dederics, and H. Katayama-Yoshida, Curie temperatures of III–V diluted magnetic semiconductors calculated from first principles, Europhys. Lett. **61**, 403 (2003).

[58] M. Kurniawan, A. Perrin, P. Xu, V. Keylin, and M. McHenry, Curie Temperature Engineering in High Entropy Alloys for Magnetocaloric Applications, IEEE Magn. Lett. **7**, 1 (2016).

[59] D. Weller, H. Brändle, G. Gorman, C.-J. Lin, and H. Notarys, Magnetic and magneto-optical properties of cobalt-platinum alloys with perpendicular magnetic anisotropy, Appl. Phys. Lett. **61**, 2726 (1992).

[60] A. Sakuma, Electronic Structure and Magnetocrystalline Anisotropy Energy of MnAl, J. Phys. Soc. Jpn. **63**, 1422 (1994).

[61] J. Lyubina, I. Opahle, K.-H. Müller, O. Gutfleisch, M. Richter, M. Wolf, and L. Schultz, Magnetocrystalline anisotropy in $L1_0$ FePt and exchange coupling in FePt/Fe_3Pt nanocomposites, J. Phys. Condens. Matter **17**, 4157 (2005).

[62] D. A. Gilbert, J.-W. Liao, L.-W. Wang, J. W. Lau, T. J. Klemmer, J.-U. Thiele, C.-H. Lai, and K. Liu, Probing the A1 to $L1_0$ transformation in FeCuPt using the first order reversal curve method, APL Mater. **2**, 086106 (2014).

[63] J. B. Kruskal, Nonmetric multidimensional scaling: A numerical method, Psychometrika **29**, 115 (1964).